J. Fluid Mech. (2019), *vol.* 880, *pp.* 1020–1035. © Cambridge University Press 2019
doi:10.1017/jfm.2019.735

A simple vortex-loop-based model for unsteady rotating wings

Juhi Chowdhury[1] **and Matthew J. Ringuette**[1,†]

[1]Department of Mechanical and Aerospace Engineering, University at Buffalo, The State University of New York, NY 14260, USA

(Received 18 March 2019; revised 15 July 2019; accepted 1 September 2019; first published online 18 October 2019)

An analytical model is developed for the lift force produced by unsteady rotating wings; this configuration is a simple representation of a flapping wing. Modelling this is important for the aerodynamic and control-system design for bio-inspired drones. Such efforts have often been limited to being two-dimensional, semi-empirical, sometimes computationally expensive, or quasi-steady. The current model is unsteady and three-dimensional, yet simple to implement, requiring knowledge of only the wing kinematics and geometry. Rotating wings produce a vortex loop consisting of the root vortex, leading-edge vortex, tip vortex and trailing-edge vortex, which grows with time. This is modelled as a tilted planar loop, geometrically specified by the wing size, orientation and motion. By equating the angular impulse of the vortex loop to that of the fluid volume driven by the wing, the circulatory lift force is derived. Potential flow theory gives the fluid-inertial lift. Adding these two contributions yields the total lift formula. The model shows good agreement with a range of experimental and computational cases. Also, a steady-state lift model is developed that compares well with previous work for various angles of attack.

Key words: swimming/flying, vortex dynamics, separated flows

1. Introduction

Unsteady and bio-inspired aerodynamics have been studied extensively, motivated by their applications to small agile drones. Research on mathematical models for vehicle design and flight controllers is ongoing, due to the challenge of representing the separated flow and the forces that a vehicle may encounter during a high-angle-of-attack manoeuvre, gust or flapping-wing motion. Here we review prior models, particularly for wings in unsteady rotation that are relevant to flapping-wing flight.

Several researchers have used potential flow theory to obtain the force and moment for the incompressible flow around a flat plate or airfoil (e.g. Ansari, Żbikowski & Knowles 2006*a*; Xia & Mohseni 2013; Yan, Taha & Hajja 2014). Using the Joukowski transformation to map the flow to a complex plane, the velocity potentials are calculated for the background flow and any singularities, such as vortices, introduced. The pressure is evaluated from the unsteady Bernoulli equation and the force can be

† Email address for correspondence: ringum@buffalo.edu

https://doi.org/10.1017/jfm.2019.735 Published online by Cambridge University Press

calculated from the unsteady Blasius theorem (see Xia & Mohseni 2013; Yan *et al.* 2014), or directly from Kelvin's impulse theorem (Ansari *et al.* 2006*a*). Eldredge & Jones (2019) suggest separately modelling the fluid-inertial or added-mass force, and the circulatory force (see also Babinsky *et al.* 2016).

One type of two-dimensional (2-D) potential-flow modelling introduces point or discrete vortices at small time intervals and advects them to model the separated shear layers, e.g. their rollup into leading-edge vortices (LEVs) (Ansari *et al.* 2006*a*; Xia & Mohseni 2013; Eldredge & Jones 2019). To solve for the unknown vortex strengths, Kelvin's theorem coupled with conditions at the leading edge (LE) and trailing edge (TE) are enforced. The Kutta condition is typically used at the TE (see Ansari *et al.* 2006*a*; Xia & Mohseni 2013; Eldredge & Jones 2019). Ramesh *et al.* (2014) defined an empirically determined LE suction parameter for rounded edges, which allows non-zero suction versus a Kutta condition, to determine LEV shedding. Li & Wu (2016) used residual vortex sheets at the LE and TE, and created maps showing the contribution of each vortex element to the plate force. Numerical methods are required to implement these discrete vortex models.

To extend this to three-dimensional (3-D) flow, for a flapping (rotating, plunging and pitching) wing Ansari *et al.* (2006*a*) and Ansari, Żbikowski & Knowles (2006*b*) used a blade-element approach, with several 2-D sections of constant radius across the wing span; integration of the sectional forces yields the total lift. Tip effects and spanwise flow are neglected, which is reasonable at a Reynolds number (Re) of 160 (calculated using mean chord and mean tip speed) (Ansari *et al.* 2006*b*). Compared to an experiment, the model accuracy for the overall mean lift is 13 %, with greater deviations in peak lift, and the mean error reduces to ∼7 % with further periodic cycles.

The inviscid 3-D unsteady vortex–lattice method (UVLM) (see Roccia *et al.* 2013; Nguyen *et al.* 2016) is also used because of its lower computational cost and higher fidelity versus the discrete vortex method. In UVLM, the vortex structures (bound vortices, wake and LEV) are divided into small lattices of constant strength, and then the velocity field is determined by applying the Biot–Savart law to the lattices. Finally, the pressure is calculated from Bernoulli's equation to obtain the force. The UVLM (Roccia *et al.* 2013) performs better than the Ansari *et al.* (2006*b*) model, which is fundamentally the 2-D version of UVLM, and works for different insect geometries and kinematics. Nguyen *et al.* (2016) further modified it to incorporate the LEV force and vortex-core growth.

Other analytical models are discussed here. For a flapping wing in hover with rotation, pitching and plunging, Żbikowski (2002) proposed two analytical approaches for calculating the lift. One is the unsteady thin-airfoil theory of von Kármán & Sears (1938), augmented with a nonlinear correction for deforming vortex wakes to model the LEV. The other is a velocity-potential approach: either a frequency-domain method (Theodorsen 1935) or an indicial technique incorporating the Wagner function (Wagner 1925), in conjunction with the Polhamus (1966) LE suction model. The latter approach was modified to account for wake deformation and downwash, giving reasonable results for periodic flapping, although wing–wake interactions were not modelled (Pedersen & Żbikowski 2006). Pullin & Wang (2004) created a similarity solution for the spiral rollup of the LE and TE vortex sheets, for a 2-D flat plate at high angle of attack (α) having power-law starting-flow velocities. The sheet development is dictated by the Birkhoff–Rott equation, and the results exhibit good agreement with numerical simulations. For a similar problem, Pitt Ford & Babinsky (2013) showed that the LEV and bound circulations can be estimated by the Wagner function.

https://doi.org/10.1017/jfm.2019.735 Published online by Cambridge University Press

For 3-D flows, Wong, Gillespie & Rival (2018) proposed a shear-layer feeding model for the LEV circulation and its spanwise advection using vorticity-containing mass. The circulation feeding-rate error is 10 % when compared with delta-wing experiments. Limacher, Morton & Wood (2016) simplified the Navier–Stokes equations to predict the LEV-core streamline, which agreed well with experiments inboard of the tip. Moreover, Chen *et al.* (2018) developed a closed-form analytical expression for the LEV position and circulation for rotating wings with various shapes, by setting a free parameter for the spanwise vorticity transport.

Some of the models described above are too computationally expensive to be readily used for engineering design or control, and low-order models are meant to address this. The NATO AVT-202 effort (Ol & Babinsky 2016) gives a 2-D low-order model for flat plates undergoing translation and pitching (see also Babinsky *et al.* 2016). It uses potential flow for the added-mass force, and a scaled Wagner function for the circulation of the LE–TE vortex dipole; the time-varying distance between the LEV and trailing-edge vortex (TEV) is approximated using a relative 'drift' velocity between their cores equal to half the free-stream velocity. Hemati, Eldredge & Speyer (2014) optimized the point-vortex strengths of the Wang & Eldredge (2013) model using high-fidelity simulation data, which yields better results. Eldredge & Darakananda (2015) also created a low-order 3-D model that represents the flow as a small number of large-scale closed vortex loops made of linear segments. The problem is open, but can be closed with further submodels (e.g. the Kutta condition) or empirical data to obtain the time-varying vortex strengths. Recently, Darakananda & Eldredge (2019) developed a 2-D model for bodies at high α, representing the LE and TE separated shear layers as discrete vortices, but the rolled-up and shed vortices as single points. To compensate for the force change from feeding circulation to the single points, a generalization of the 'impulse-matching' approach (Wang & Eldredge 2013) to alter the point-vortex velocities is used.

Semi-empirical low-order models include that of Mancini, Manar & Jones (2015) for high-α translating and pitching plates. The potential-flow model incorporates LEV position and strength from experiments, and the steady-state lift coefficient is used to scale down the overpredicted lift. The accuracy is within 20 % when the vortex tracking is reliable, prior to LEV dissipation. A recent paper presents a cycle-averaged semi-empirical force model for a plunging (out-of-plane rotation) and twisting wing based on an undulating wave model applied to actuator disk theory (Jiao *et al.* 2018). The thrust force is a simple algebraic expression, somewhat similar to the circulatory lift developed in this paper and will be discussed in § 2. Galler, Weymouth & Rival (2019) proposed a semi-empirical model for an accelerating plate based on Darwin's drift-volume approach. They also discussed the limitations of decomposing the unsteady force into circulatory and non-circulatory components for highly separated flows during the acceleration phase.

In general, quasi-steady models use steady-state forces from experiments or computational fluid dynamics (CFD) at different instants of the wing motion to estimate the time-varying lift (see Sane & Dickinson 2002; Berman & Wang 2007; Percin & van Oudheusden 2015). Sane & Dickinson (2002) presented a quasi-steady model and blade-element implementation for a flapping wing undergoing rotation and pitching. Lee *et al.* (2016*b*) expanded this model to a greater variety of wing kinematics and geometries by finding coefficients using curve fitting to CFD simulations; the error was generally within 10 %, but up to 20 % in some cases. Nabawy & Crowther (2014) improved the Sane & Dickinson (2002) model by introducing a power factor $k = k_{ind}k_{tip}k_{flap}$ in Prandtl's lifting line theory, to estimate the

https://doi.org/10.1017/jfm.2019.735 Published online by Cambridge University Press

slope of the 3-D wing lift. The k_{ind}, k_{tip} and k_{flap} represent the non-uniform downwash velocity, tip loss and effective flapping disk area, respectively, and can be evaluated analytically. Berman & Wang (2007) presented force and moment expressions based on the Navier–Stokes equations with quasi-steady models for the circulatory and viscous terms, for a flapping wing (rotation, pitch and plunge). This formulation was convenient for energy optimization and a sensitivity analysis of the parameters.

A state-space model given by Taha, Hajja & Beran (2014) uses Duhamel's principle assuming linearity of the unsteady aerodynamics around flapping wings (rotation and pitching). Stipulating an attached LEV, the static lift is found from a semi-empirical relation involving aspect ratio ($\mathcal{AR}$) and α. Coupled with the Wagner function, the unsteady lift is calculated. To make the model low-order, the radius of gyration is taken as the representative wing length. The model error is within 13 % of the direct numerical simulation results. Lee, Choi & Kim (2015) developed a simple scaling law for the lift using a steady vortex-loop theory, where the LEV circulation is scaled by that around a finite-$\mathcal{AR}$ wing. It uses only kinematic and geometric parameters, and produces an excellent collapse of the lift data for various hovering insects. The final expression is the closest to that presented here; however, the current approach employs an unsteady physical model of the evolving wing-vortex loop.

There remains a lack of a rotating-wing model that is 3-D, unsteady, closed-form, analytical and very inexpensive. In this paper, we present a simple model having these qualities, using vortex-loop dynamics. Several researchers showed that the rotating wing produces a vortex loop containing the LEV, tip vortex (TV), TEV and root vortex (RV) (e.g. Sun & Wu 2004; Kim & Gharib 2010; Ozen & Rockwell 2012*b*). Substantial advances have been made in understanding vortex-loop dynamics, especially for vortex rings (see Shariff & Leonard 1992). Sullivan *et al.* (2008) established straightforward relations among the vortex-ring parameters, such as velocity, radius, circulation, etc., and vortex generator. This motivated the current study to estimate the unsteady lift, which takes advantage of the coherent vortex loop produced in rotating-wing flow, avoids complications from the 3-D flow structures, yet retains key physics. The model is presented in § 2, and in § 3 we compare it to several experiments and numerical simulations.

2. Model

Here the incompressible flow of a rectangular wing rotating from rest at a fixed, high α is modelled as a single tilted LEV–TV–TEV–RV loop. The impulse of a thin, 3-D vortex loop can be written in a simple form (Wu, Ma & Zhou 2006) as

$$\boldsymbol{I} = \rho \Gamma \boldsymbol{S}, \tag{2.1}$$

where ρ is the fluid density, Γ is the loop circulation and $\boldsymbol{S}$ is the vector surface spanned by the loop. Once the impulse is known, the net force on the wing in the vertical direction, or lift, can be calculated as

$$L = L_{in} + \rho \frac{\mathrm{d}}{\mathrm{d}t}(\Gamma S_{hor}), \tag{2.2}$$

where S_{hor} is the projection of the loop area onto the horizontal plane. The second term on the right-hand side is similar to that found in Wu *et al.* (2006). The two contributions to the net lift are the fluid-inertial force and circulatory force. Here, assuming an infinitely thin flat-plate wing, potential flow theory (Sedov 1965) is used

https://doi.org/10.1017/jfm.2019.735 Published online by Cambridge University Press

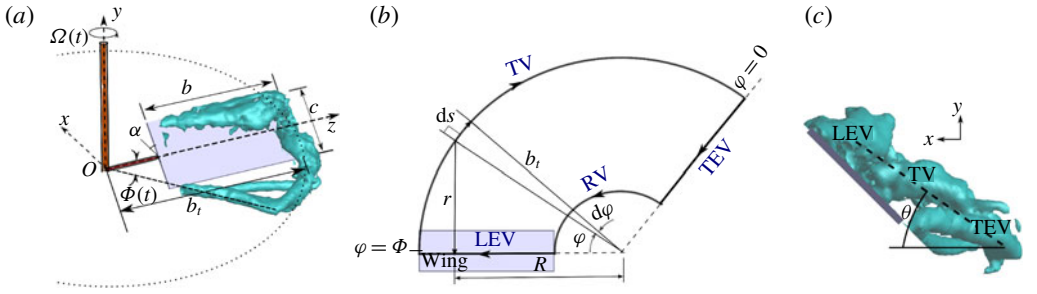

FIGURE 1. (Colour online) (*a*) Schematic of the model wing and its motion, including a $\mathcal{Q}^* = 6$ isosurface (Carr *et al.* 2015) to illustrate the real vortex loop. (*b*) Simplified vortex-loop geometry for the model (top view); the loop arrows give the swirl direction. (*c*) Experimental visualization to conceptually show the model loop angle (θ).

at each wing section to calculate the fluid-inertial lift per unit span. This can be integrated over the entire span to get the net fluid-inertial lift, which for a rectangular, rotating wing is (Percin & van Oudheusden 2015)

$$L_{in} = \pi\rho c^2 \ddot{\Phi} \frac{b_t^2 - (b_t - b)^2}{8} \sin\alpha\cos\alpha, \tag{2.3}$$

where Φ is the wing rotation angle, $\ddot{\Phi}$ is the angular acceleration, c is the chord, b is the span, b_t is the total span, including the root cutout or offset, and α is the geometric angle of attack (figure 1*a*). For the rectangular wings considered here, $\mathcal{AR} = b/c$.

Figure 1(*a*) also shows an isosurface of the $\mathcal{Q}$-criterion from the $\mathcal{AR} = 2$ experiments of Carr, DeVoria & Ringuette (2015), to illustrate the real vortex flow for comparison with the model. Here the dimensionless $\mathcal{Q}^* = \mathcal{Q}c^2/(R\Omega)^2$ is used, where R is the radius of gyration and Ω is the angular speed. A top view of the rotating-wing LEV–TV–TEV–RV loop geometry for the present model is given in figure 1(*b*). It is a simplification of the experiments and simulations mentioned in § 1, including that of figure 1(*a*). At the start of rotation, $\Phi = 0$, the LEV and TEV are collocated at the span-parallel line (z-axis), which intersects the axis of rotation, making the initial loop area zero. The z-axis moves with the wing as $\Phi(t)$ increases. It is assumed that there is a single LEV from root to tip that remains attached at this z-axis during wing rotation, discussed further below. The TEV stays fixed at the starting angular position, which is an approximation of the behaviour found by Carr *et al.* (2015). For the model, the TV and RV formation follow the arcs traversed by the z-axis, at their respective edge locations, starting from $\Phi = 0$. Therefore, the loop shape is a circular sector growing with $\Phi(t)$, minus the root-cutout region.

Piston–cylinder vortex-generator experiments have shown that the momentum imparted by the piston to the volume of fluid it displaces is nearly equal to the impulse of the vortex ring (Sullivan *et al.* 2008). Drawing an analogy to the rotating-wing configuration, we assume that the angular impulse of the vortex loop about the axis of wing rotation is equal to the angular momentum of the volume of fluid brought into motion by the wing,

$$m_f R^2 \overline{\Omega} = \rho \Gamma S_{ver} R, \tag{2.4}$$

https://doi.org/10.1017/jfm.2019.735 Published online by Cambridge University Press

where m_f is the mass of this fluid, and the associated volume is approximated as the area swept through by the wing in the horizontal plane, multiplied by the projection of the wing chord onto the vertical plane,

$$m_f = \frac{1}{2}\rho(c\sin\alpha)(b_t^2 - (b_t - b)^2)\Phi. \tag{2.5}$$

In (2.4), the radius of gyration can be calculated from (2.6) for rectangular plates (Lee, Lua & Lim 2016*a*):

$$R = c\sqrt{\frac{\left(\dfrac{b_t - b}{c} + \mathcal{AR}\right)^3 - \left(\dfrac{b_t - b}{c}\right)^3}{3\mathcal{AR}}}. \tag{2.6}$$

Similar to the mean piston speed in the momentum conservation equation of Sullivan *et al.* (2008), the running mean of the angular speed, $\overline{\Omega}(t)$, is used in (2.4), i.e. at each time the mean is calculated starting from $t = 0$ (Gharib, Rambod & Shariff 1998):

$$\overline{\Omega}(t) = \frac{1}{t}\int_0^t \Omega(\tau)\,\mathrm{d}\tau = \frac{\Phi(t)}{t}. \tag{2.7}$$

The S_{ver} in (2.4) is the projection of the vortex loop area onto the vertical plane, derived later.

As mentioned above, it is assumed that the LEV stays attached along the z-axis (or the wing) until the end of the motion. Jardin & Colonius (2018) showed that this is true approximately for a local Rossby number, Ro, of $Ro = z/c < 3$, if the span is long enough to avoid nearby TV effects (see also Lentink & Dickinson 2009; Kruyt *et al.* 2015). For larger z/c, the LEV moves farther aft and interacts with the trailing tip flow. The LEV evolution depends on Re, $\mathcal{AR}$ and Ro (see Bhat *et al.* (2019), who determined that these effects are best isolated using span-based definitions of Re and Ro), but often exhibits arch-like liftoff outboard and further LEVs forming ahead of the main one (e.g. Jardin, Farcy & David 2012; Harbig, Sheridan & Thompson 2013; Garmann & Visbal 2014; Carr *et al.* 2015; Percin & van Oudheusden 2015; Phillips, Knowles & Bomphrey 2015; Lee *et al.* 2016*a*; Bhat *et al.* 2019). However, the LEV remains close to the wing over much of the span and the overall flow exhibits a growing vortex loop for up to $\mathcal{AR} \approx 4$, albeit with complex outboard structures (Garmann & Visbal 2014; Carr *et al.* 2015; Jardin & Colonius 2018). Therefore, the simplified assumptions of an attached LEV and large-scale, increasing loop structure are reasonable at least for the $\mathcal{AR}$ values tested in § 3. Taking advantage of this, S_{hor} is calculated as the area traversed by the z-axis in the horizontal plane (figure 1*b*):

$$S_{hor} = \frac{1}{2}(b_t^2 - (b_t - b)^2)\Phi. \tag{2.8}$$

The S_{hor} therefore increases linearly with Φ, as also found by Sun & Wu (2004). For simplicity, the additional wing area is neglected, since including it produces a negligible change in lift. Moreover, placing the LEV at the z-axis reduces the complexity of the Biot–Savart calculation, given below.

As shown in simulations and experiments, the vortex loop is inclined but with a complex, unsteady 3-D geometry (Sun & Wu 2004; Carr *et al.* 2015; Jardin &

https://doi.org/10.1017/jfm.2019.735 Published online by Cambridge University Press

Colonius 2018). This is represented in the model by a single angle $\theta(\Phi)$ with respect to the horizontal (figure 1*c*), yielding a planar loop. The θ is necessary to calculate S_{ver}:

$$S_{ver} = \tfrac{1}{2}(b_t^2 - (b_t - b)^2)\Phi \tan\theta. \tag{2.9}$$

From (2.4), Γ can then be solved:

$$\Gamma = \frac{R\overline{\Omega} c \sin\alpha}{\tan\theta}. \tag{2.10}$$

Lee *et al.* (2015) give a similar expression, but for steady circulation, using a scaling law. The dynamic, 3-D nature of the real vortex loop makes it challenging to model θ. For simplicity, we conceptualize θ as being dictated by α^*, which is α scaled by the near-wake flow, and the angle α_i produced by the induced velocity of the loop itself:

$$\theta(\Phi) = \alpha^* - \alpha_i(\Phi). \tag{2.11}$$

The α^* term is meant to account for the flow deflection after it passes over the wing. First, we take a reference for the deflection angle to be $\alpha = \arctan(\sin\alpha/\cos\alpha)$, i.e. aligned with the chord line. However, prior work shows that the TE flow does not follow the chord line after it leaves the wing for all α. For example, at large α, such as 60°, the TE flow deflects upwards compared to the chord line (Ozen & Rockwell 2012*a*; Garmann & Visbal 2014; Li, Dong & Cheng 2017), implying a reduction of the near-wake downward flow. At smaller α, e.g. 15°, there is evidence that the TE flow is below this line (Jones & Babinsky 2011; Li *et al.* 2017). To capture this inverse relationship of the near-wake downward flow with α, the $\sin\alpha$ is divided by the vertical deflection velocity, V_1, from the wing orientation with a scaling factor K to be determined, i.e. $V_1 = KR\Omega\sin\alpha$. Also, this can be thought of as accounting for the downwash from the LEV in the near-wake region. Similarly, the $\cos\alpha$ is divided by the approximate horizontal velocity of the TEV, V_2, in the wing-fixed frame, which is estimated to be $R\Omega$ as discussed above. Effectively, this does not adjust the horizontal flow path, but achieves the desired decrease in the vertical flow deflection with increasing α for a more physically meaningful α^*. Overall, the expression is

$$\alpha^* = \arctan\left(\frac{V_2}{V_1}\frac{\sin\alpha}{\cos\alpha}\right) = \arctan\left(\frac{R\Omega}{KR\Omega\sin\alpha}\frac{\sin\alpha}{\cos\alpha}\right) = \arctan\left(\frac{1}{K\cos\alpha}\right). \tag{2.12}$$

The K estimation is motivated by observations from the $\alpha = 45°$, $\mathcal{R} = 2$ rotating-wing data of Carr *et al.* (2015). Figure 2(*a*) shows velocity vectors in the rotating frame in an x–y plane at the radius of gyration, for $\Phi = 84°$. In the near wake, the vectors are roughly aligned with the wing chord line, as illustrated by the dashed 45° reference line in figure 2(*a*), although there are local spatial variations as expected. This indicates that at $\alpha = 45°$ the near-wing wake flow can be approximated as being aligned with the chord, so that $\alpha^* \approx \alpha$. The ratio of the near-wake downward velocity to the horizontal reference velocity, $v/(R\Omega)$, is visualized in three dimensions in figure 2(*b*) using three isosurfaces: $v/(R\Omega) = -1.0$ and -0.9, and $\mathcal{Q}^* = 6$ showing the vortex structure. There is a coherent region of magnitude $v/(R\Omega) \sim 1$ in the wake

https://doi.org/10.1017/jfm.2019.735 Published online by Cambridge University Press

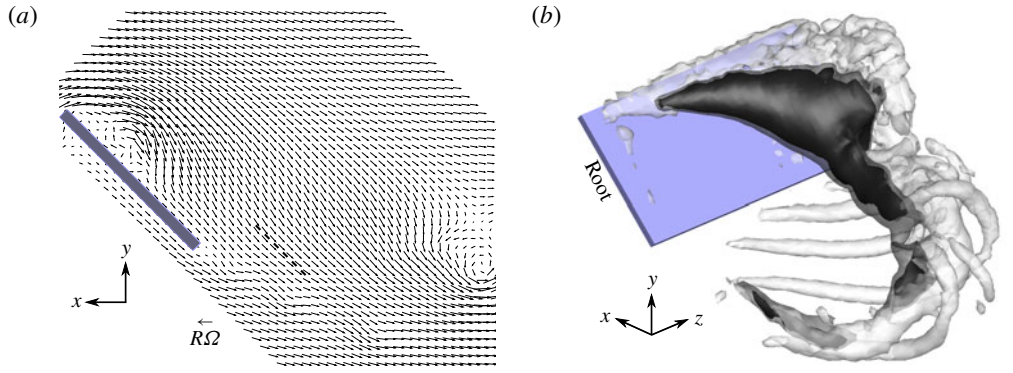

FIGURE 2. (Colour online) Experimental results from Carr *et al.* (2015) for $\mathcal{AR} = 2$, $\alpha = 45^\circ$ and $\Phi = 84^\circ$ motivating α^*. (*a*) Wing-fixed x–y plane velocity vectors at R along the wing span (every other vector is given); a dashed 45° line is in the near wake for reference. (*b*) Isosurfaces showing magnitudes of downward velocity and the vortex loop: nested black and translucent grey indicate $v/(R\Omega) = -1.0$ and -0.9, respectively; translucent white is $\mathcal{Q}^* = 6$.

near the radius of gyration. This further suggests that the assumption of $\alpha^* \approx \alpha$ is plausible for $\alpha = 45^\circ$. Wolfinger & Rockwell (2015) also showed regions of magnitude ~ 1 dimensionless downward velocity in the outboard flow of an $\mathcal{AR} = 2$, $\alpha = 45^\circ$ wing for high Φ and slightly larger R/c. Therefore, the assumption of $\alpha^* \approx \alpha$ at $\alpha = 45^\circ$ leads to $K = \sqrt{2}$. Although K is estimated from observations at only $\alpha = 45^\circ$ and $\mathcal{AR} = 2$, § 3 shows that α^* and α_i yield a θ that allows the model to capture the correct lift trend with α.

The induced angle α_i is given by

$$\tan \alpha_i = \left| \frac{v_i}{U_{hor}} \right| = \frac{\Gamma A}{\left| R\overline{\Omega} - \Gamma A \tan \theta \right|} \approx \frac{\Gamma A}{R\overline{\Omega}}. \tag{2.13}$$

Here v_i is the downward induced velocity, U_{hor} is the net horizontal velocity at R from the wing motion and induced by the loop, and ΓA is the induced velocity of the horizontally projected loop itself; A is what remains after Γ is factored out of the Biot–Savart calculation. The denominator $|R\overline{\Omega} - \Gamma A \tan \theta|$ can be approximated as $R\overline{\Omega}$, since $R\overline{\Omega} \gg \Gamma A \tan \theta$.

The A is evaluated on the z-axis at R using the Biot–Savart law at each instant in time (Γ is assumed constant along the loop):

$$\Gamma \boldsymbol{A} = \frac{\Gamma}{4\pi} \int_{loop} \frac{\mathrm{d}\boldsymbol{s} \times \boldsymbol{r}}{|\boldsymbol{r}|^3}, \tag{2.14}$$

where $\mathrm{d}\boldsymbol{s}$ is a differential length element along the loop, and $\boldsymbol{r}$ is the position vector from the loop to the point R. This calculation is done for the TV, RV and TEV loop segments, and for illustration figure 1(*b*) gives the parameters for the TV contribution. The reference position R is taken for U_{hor} and the A calculation, since it has been shown to be the most appropriate wing length scale when non-dimensionalizing and comparing flapping-wing data (Lee *et al.* 2016*a*). The magnitude A is

$$A = A_{RV} + A_{TV} + A_{TEV}, \tag{2.15}$$

https://doi.org/10.1017/jfm.2019.735 Published online by Cambridge University Press

where

$$A_{RV} = \left| \frac{1}{4\pi} \int_0^{\Phi(t)} (b_t - b) \frac{(b_t - b) - R\cos\varphi}{(R^2 + (b_t - b)^2 - 2R(b_t - b)\cos\varphi)^{3/2}} \,\mathrm{d}\varphi \right|, \tag{2.16}$$

$$A_{TV} = \left| \frac{1}{4\pi} \int_0^{\Phi(t)} b_t \frac{b_t - R\cos\varphi}{(R^2 + b_t^2 - 2Rb_t\cos\varphi)^{3/2}} \,\mathrm{d}\varphi \right|, \tag{2.17}$$

$$A_{TEV} = \left| \frac{1}{4\pi} \int_0^{b} \frac{R\sin\Phi}{(R^2 + (b_t - \beta)^2 - 2R(b_t - \beta)\cos\Phi)^{3/2}} \,\mathrm{d}\beta \right|. \tag{2.18}$$

The modulus is used so the result is consistent with the actual integration path direction. The integrals are of the elliptic form, and therefore can be evaluated analytically. However, in § 3, integrals and derivatives are calculated numerically (trapezoidal rule and second-order least-squares differentiation, respectively) for convenience.

Early in the motion, A_{TEV} (2.18) has a very high value because of the proximity of the LEV to the TEV. However, afterwards, A_{TEV} is very small compared to A_{TV}. Therefore, equation (2.15) is approximated as

$$A = A_{RV} + A_{TV}. \tag{2.19}$$

Then, substituting (2.10), (2.12), (2.13) and (2.19) into (2.11) gives

$$\sqrt{2}\cos\alpha\tan^2\theta + (Ac\sin\alpha - 1)\tan\theta + \sqrt{2}Ac\sin\alpha\cos\alpha = 0. \tag{2.20}$$

The root of (2.20) that is physically meaningful is

$$\tan\theta = \frac{1}{2\sqrt{2}\cos\alpha}\left[-(Ac\sin\alpha - 1) + \sqrt{(Ac\sin\alpha - 1)^2 - 8Ac\sin\alpha\cos^2\alpha}\right]. \tag{2.21}$$

Later in the motion, for high Φ such as 200° (depending on the wing geometry and kinematics), the root fails and so $\mathrm{d}\theta/\mathrm{d}t$ is frozen thereafter. Once θ is known, Γ is calculated using (2.10). Finally, the Γ, S_{hor} (2.8) and L_{in} (2.3) are substituted into (2.2) to compute the time-varying lift. The time average of the $\rho\,\mathrm{d}(\Gamma S_{hor})/\mathrm{d}t$ term of (2.2) yields a similar expression to that of Jiao *et al.* (2018) for the cycle-averaged thrust of a flapping wing (plunging and twisting) with no root gap. It should be further noted that the current model only requires the wing geometry and kinematics as inputs.

Additionally, a steady-state lift expression is developed from (2.2). Using (2.10) and (2.8), the circulatory lift component, L_{circ}, can be written as

$$\begin{aligned} L_{circ} &= \rho\frac{\mathrm{d}}{\mathrm{d}t}(\Gamma S_{hor}) \\ &= \frac{1}{2}R\rho c\sin\alpha(b_t^2 - (b_t - b)^2)\left[\frac{2\Phi\,\mathrm{d}\Phi/\mathrm{d}t}{t\tan\theta} - \frac{\Phi^2}{t^2\tan\theta} - \frac{\Phi^2\,\mathrm{d}\theta/\mathrm{d}t}{t\sin^2\theta}\right]. \end{aligned} \tag{2.22}$$

At steady state, $\mathrm{d}\Phi/\mathrm{d}t$ and Φ/t can be individually equated to Ω_f, where Ω_f is the final steady angular speed, and $\mathrm{d}\theta/\mathrm{d}t = 0$. The steady-state value for $\tan\theta$ requires the steady-state value of A, which can be determined by assuming the TV and RV to be semi-infinite in length, with circulation Γ. The corresponding induced velocity due to both vortices is still calculated at R, giving A_{ss} as

$$A_{ss} = \frac{1}{4\pi}\left[\frac{1}{b_t - R} + \frac{1}{R - (b_t - b)}\right], \tag{2.23}$$

https://doi.org/10.1017/jfm.2019.735 Published online by Cambridge University Press

Cases	$\mathcal{AR}$	Root cutout $(b_t - b)/c$	α (deg.)	R/c	Angle (deg.) travelled during acceleration	Re (based on $U_{R,f}$ and c)
UB4	4	0.3	45	2.57	10 ($R\Phi = 0.45$c)	1609
UB3	3	0.3	45	2.00	10 ($R\Phi = 0.35$c)	3312
UB2	2	0.3	45	1.42	10 ($R\Phi = 0.24$c)	3558
TUD	2	0.7	45	1.80	27 ($R\Phi = 0.85$c)	8113
UMD-fast	2	0.5	45	1.60	32 ($R\Phi = 0.90$c)	17 071
UMD-slow	2	0.5	45	1.60	187 ($R\Phi = 5.24$c)	17 071
RVC	2	0.5	45	1.60	187 ($R\Phi = 5.24$c)	660
AFRL	2	0.5	60	1.60	43 ($R\Phi = 1.22$c)	3215

TABLE 1. Cases for model validation.

where the first and second terms on the right-hand side are due to the TV and RV, respectively. At steady state, $\tan\theta$ becomes

$$\tan\theta_{ss} = \frac{1}{2\sqrt{2}\cos\alpha}\left[-(A_{ss}c\sin\alpha - 1) + \sqrt{(A_{ss}c\sin\alpha - 1)^2 - 8A_{ss}c\sin\alpha\cos^2\alpha}\right]. \tag{2.24}$$

Finally, the steady-state values are substituted into (2.22), and L_{circ} is non-dimensionalized by $1/2\rho U_{R,f}^2 bc$ to get the steady-state lift coefficient, $C_{L,ss}$, where $U_{R,f}$ is the final azimuthal velocity at R:

$$C_{L,ss} = \frac{(2b_t - b)\sin\alpha}{R\tan\theta_{ss}}. \tag{2.25}$$

3. Model validation and discussion

We consider six different experimental cases to validate the model, namely $\mathcal{AR} = 2$, 3 and 4 from Carr *et al.* (2015), here called UB2, UB3 and UB4, respectively, and $\mathcal{AR} = 2$ with slower accelerations and varying root cutouts from Manar *et al.* (2016) (UMD-fast) and Percin & van Oudheusden (2015) (TUD). We also compare the model with the more gradual acceleration experiment of Manar *et al.* (2016), called UMD-slow. Additionally, we test it against the computational simulation of Phillips, Nakata & Bomphrey (found in Jones *et al.* 2016) with a motion profile and geometric parameters matching those of UMD-slow, and that of Garmann & Visbal (2014), here referred to as RVC and AFRL, respectively. The motion for the AFRL case is very gradual in the beginning, and we consider the start of the motion for the model at $\Phi \approx 1°$. All unsteady cases tested have $\alpha = 45°$, except for AFRL with $\alpha = 60°$. Further, steady-state model results are compared with the experiments of Dickinson, Lehmann & Sane (1999) for various α.

Figure 3(*a*) gives the motion profiles for all unsteady cases, and table 1 provides their specific parameters. The force data were extracted from plots in the references and interpolated to a discrete time scale for all cases except the Carr *et al.* (2015) results, which were directly available. The motion profiles were generated from the equations used in the references. Figure 3(*b*) shows how the model loop angle θ varies with Φ for all cases. The θ starts from a value equal to α^*, then decreases rapidly and finally becomes nearly constant. All $\mathcal{AR} = 2$ cases have comparable loop angles for the same α.

https://doi.org/10.1017/jfm.2019.735 Published online by Cambridge University Press

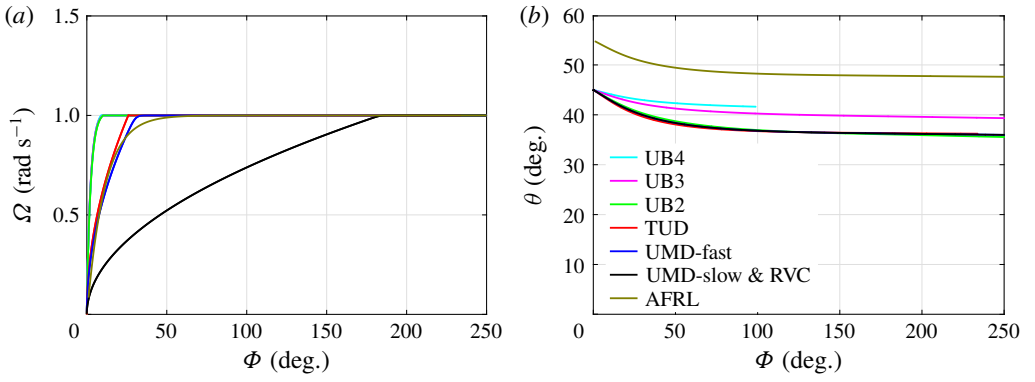

FIGURE 3. (*a*) Motion profiles; UB2, UB3 and UB4 overlap. (*b*) Loop angle variation.

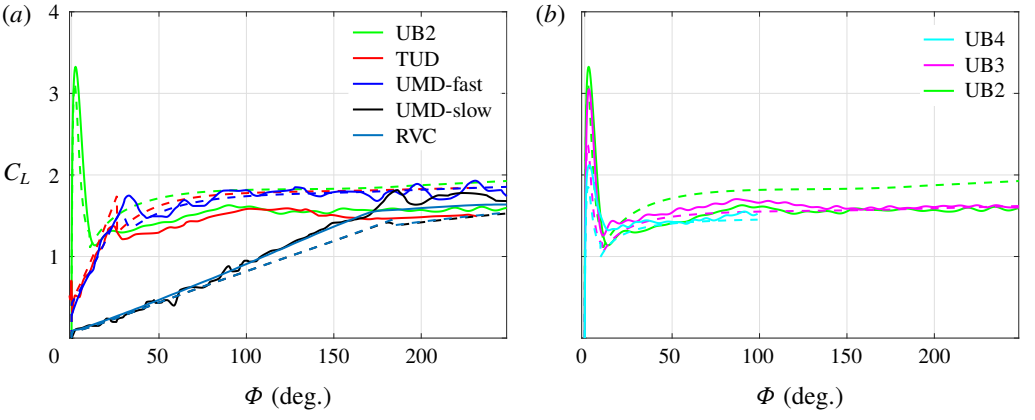

FIGURE 4. Comparison of the lift coefficient from the $\alpha = 45^\circ$ experimental/numerical cases (solid lines) and the model (dashed lines): (*a*) $\mathcal{R} = 2$ and (*b*) $\mathcal{R} = 2$–4.

The lift coefficients, $C_L = 2L/\rho U_{R,f}^2 bc$, for all $\mathcal{R} = 2$ and $\alpha = 45^\circ$ cases are shown in figure 4(*a*) and those for the different $\mathcal{R}$ tests of Carr *et al.* (2015) are given in figure 4(*b*). Figure 5(*a*) presents the C_L comparison for $\alpha = 60^\circ$. The model reasonably predicts C_L within 18 % of the experimental results during the wing's steady motion, except for TUD and UB2, which have maximum errors below 27 %. It is not always effective at capturing the startup-acceleration peak, and the deviation is more than 20 % of the experimental results. However, it gives a reasonable estimate (within 12 % error) of the peak when compared with the numerical simulations. The model's non-circulatory force component starts to decrease from the peak value before the experimental C_L drops for all cases, possibly because of force-signal filtering and also in the experiment the fluid's inertia continues to exert force past the instant the wing acceleration ceases (Galler *et al.* 2019).

The model force could be affected at some time instants by the simplifications. For example, a single loop angle θ is used to represent the orientation of the complex 3-D loop structure; this could incur some error. Also, in determining α^*, the tangent of the geometric α is scaled by the ratio of vertical and horizontal velocities at R, estimated based on observations from experiments/simulations in the near-wake region.

https://doi.org/10.1017/jfm.2019.735 Published online by Cambridge University Press

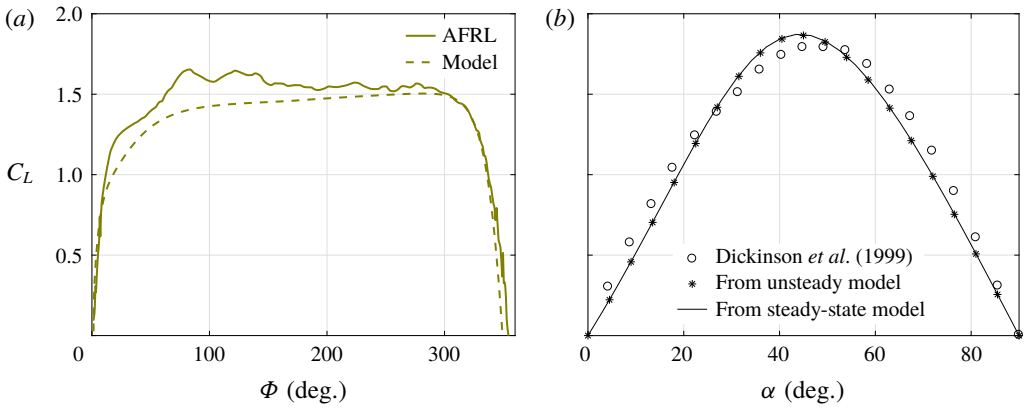

FIGURE 5. (Colour online) (*a*) Unsteady C_L versus Φ: $\mathcal{AR} = 2$ and $\alpha = 60°$. (*b*) Steady-state C_L versus α: $\mathcal{AR} = 2$.

Cases	UB4	UB3	UB2	TUD	UMD-fast	UMD-slow	RVC	AFRL
Error (%)	6.3	3.5	16.6	18.2	4.9	10.9	7.4	9.4

TABLE 2. Model error based on mean C_L.

Perhaps this could be improved in the future with the knowledge of a detailed analysis of the flow behaviour in this region for varying α. Further, there is a range of Φ between the occurrence of high and low A_{TEV} values for which the TEV is not too close (spatially) to the LEV to make A_{TEV} go to infinity, nor too far for A_{TEV} to be insignificant compared to A_{TV} (see § 2); A_{TEV} significantly contributes to A in this region. Additionally, the presence of split or multiple outboard LEVs in the real high-Re flows, filtering of the experimental data, and set-up constraints such as mounting hardware are not captured by the model.

Overall, the model may also deviate from the experiments and simulations for the following reasons. First is the assumption that the impulse of the loop is equal to that imparted to the volume of fluid swept by the wing. Sullivan *et al.* (2008) presented the ratio of impulses measured in an experiment to those calculated from their piston–cylinder model, which uses the same assumption. The impulse is over- or underpredicted up to 10 % for the cases considered (cf. their table 8). Second, the vortex loop area is modelled here as the sector area traversed by the wing. This is a good assumption but they are not exactly equal. Despite these drawbacks, for the UB3, UB4, UMD-fast, RVC and AFRL cases, the error is within 10 % for most of the Φ range shown. Also, we calculate the error based on the mean C_L taken over Φ up to 250° for each case, as given in table 2. The deviation is within 20 % for all cases, and for some it is below 10 %.

Further, the trends of the model C_L show good agreement with those of the experiments and simulations. In all cases, C_L increases with a shallow slope even after the wing stops accelerating (figure 4*a* and 4*b*) for both the model and benchmark cases. This produces a broad local maximum in some of the experimental and numerical C_L curves, whereas in others and all the model estimations, the C_L simply levels off.

https://doi.org/10.1017/jfm.2019.735 Published online by Cambridge University Press

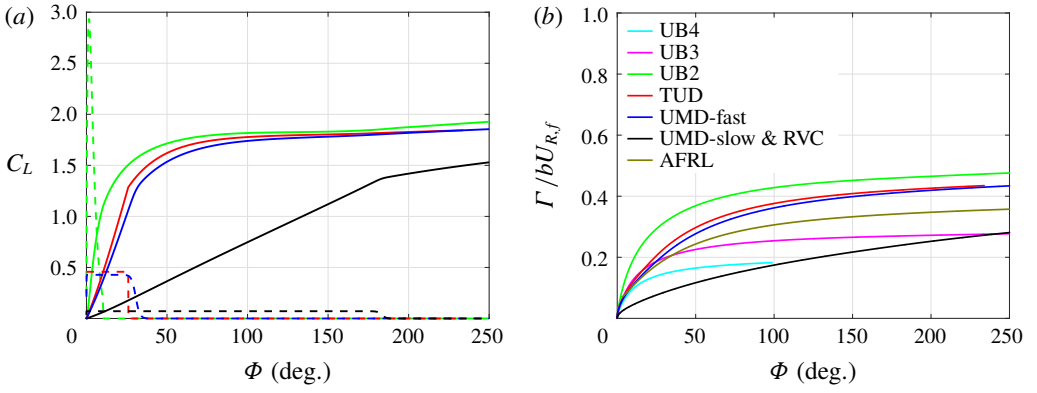

FIGURE 6. (*a*) Inertial and circulatory lift coefficients (dashed and solid lines, respectively) for the $\mathcal{AR} = 2$, $\alpha = 45^\circ$ cases. (*b*) Loop circulation for all cases.

Cases	Ac $(\Phi = 180^\circ)$	$A_{ss}c$
UB2	0.1619	0.1616
UB3	0.1092	0.1080
Dickinson *et al.* (1999)	0.1575	0.1600

TABLE 3. Comparison of dimensionless Ac and $A_{ss}c$ for cases with various $\mathcal{AR}$ and Ro.

Figure 5(*b*) gives the behaviour of the model with α, comparing the average C_L of the unsteady model over $\Phi = 150^\circ$–250°, and the steady-state form (2.25), to the quasi-steady measurements of Dickinson *et al.* (1999) for $\alpha = 0^\circ$–90°. To calculate the $C_{L,ss}$ (2.25), the unsteady A was simplified for long-time behaviour by assuming semi-infinite TV and RV to obtain A_{ss} (cf. § 2). The dimensionless $A_{ss}c$ estimate is very close to the unsteady counterpart in the steady state, as shown for some cases with various $\mathcal{AR}$ and $Ro = R/c$ in table 3. Dickinson *et al.* (1999) measured the lift for a robotic fruit-fly wing rotating from rest in a liquid-filled tank. For both the unsteady and steady models, to compare with the experiment we use a rectangular geometry but match their wing area, $\mathcal{AR} = 2$ and $Ro = 2.35$; the unsteady model employs the UB2 velocity profile. Figure 5(*b*) shows excellent agreement between the unsteady- and steady-state forms of the model, and these compare well with the quasi-steady measurements. Together with figures 4 and 5(*a*), this demonstrates that the model can predict the proper trends with α. At first the steady-state C_L increases with α, then after approximately $\alpha = 45^\circ$, it decreases to zero at $\alpha = 90^\circ$ (figure 5*b*).

In figure 6(*a*), the model inertial and circulatory force components are given for the $\mathcal{AR} = 2$, $\alpha = 45^\circ$ cases. In the steady-motion portion, eventually the circulatory forces become very close despite the differences in motion profiles. Figure 6(*b*) shows the dimensionless vortex loop circulation; b is used in scaling it to represent the loop size. The circulation initially increases with Φ; then its growth substantially reduces after wing acceleration ceases. As given by (2.10), this behaviour is governed by $\overline{\Omega}(t)$ and θ, leading to the slowing growth as they level off. The trend of the loop circulation resembles that of the total circulation produced at the LE in the Carr *et al.* (2015) experiments.

https://doi.org/10.1017/jfm.2019.735 Published online by Cambridge University Press

4. Conclusions

In this paper we present a simple analytical model for unsteady rotating-wing lift with the wing geometry and kinematics as the only inputs. The LEV is assumed to remain attached to the wing for the entire duration of the rotating motion, and to be connected to the TV, TEV and RV to form a closed loop. The wing motion specifies the shape and size of the planar loop in the model, and its tilt, as observed in experiments and numerical simulations, is determined from consideration of the wing orientation, flow deflection and downwash. By matching the angular momentum of the loop to that of the volume of fluid swept by the wing about the axis of rotation, the circulation of the loop is found. The loop area increases linearly with the angular displacement of the wing (Sun & Wu 2004). Circulation is multiplied by the loop area and density to give the impulse. Finally, the net lift force is the sum of the inertial lift from potential flow theory and the time derivative of the loop impulse. The model is compared with some experimental and computational results having different $\mathcal{AR}$, α and motion profiles. The model predicts unsteady lift reasonably well, and mean lift within 20 % deviation. Further, a steady-state form of the model is derived, which shows excellent agreement with the averaged value of the unsteady model in the steady-state part. The lift variation with α found in prior literature is also captured very well. The circulation of the vortex loop first increases and then stays approximately constant, as dictated by the running mean of the wing angular velocity and the loop tilt angle.

Acknowledgements

The authors would like to thank the anonymous referees for their valuable comments, which strengthened the paper's impact. We also acknowledge support from the National Science Foundation, award no. CBET-1706453, supervised by Dr R. Joslin.

REFERENCES

ANSARI, S. A., ŻBIKOWSKI, R. & KNOWLES, K. 2006*a* Non-linear unsteady aerodynamic model for insect-like flapping wings in the hover. Part 1: Methodology and analysis. *J. Aerosp. Engng* **220** (2), 61–83.

ANSARI, S. A., ŻBIKOWSKI, R. & KNOWLES, K. 2006*b* Non-linear unsteady aerodynamic model for insect-like flapping wings in the hover. Part 2: Implementation and validation. *J. Aerosp. Engng* **220** (3), 169–186.

BABINSKY, H., STEVENS, R. J., JONES, A. R., BERNAL, L. P. & OL, M. V. 2016 Low order modelling of lift forces for unsteady pitching and surging wings. In *54th AIAA Aerospace Sciences Meeting*. AIAA SciTech Forum (2016-0290).

BERMAN, G. J. & WANG, Z. J. 2007 Energy-minimizing kinematics in hovering insect flight. *J. Fluid Mech.* **582**, 153–168.

BHAT, S. S., ZHAO, J., SHERIDAN, J., HOURIGAN, K. & THOMPSON, M. C. 2019 Uncoupling the effects of aspect ratio, Reynolds number and Rossby number on a rotating insect-wing planform. *J. Fluid Mech.* **859**, 921–948.

CARR, Z. R., DEVORIA, A. C. & RINGUETTE, M. J. 2015 Aspect-ratio effects on rotating wings: circulation and forces. *J. Fluid Mech.* **767**, 497–525.

CHEN, D., KOLOMENSKIY, D., ONISHI, R. & LIU, H. 2018 Versatile reduced-order model of leading-edge vortices on rotary wings. *Phys. Rev. Fluids* **3** (114703), 1–13.

DARAKANANDA, D. & ELDREDGE, J. D. 2019 A versatile taxonomy of low-dimensional models for unsteady aerodynamics. *J. Fluid Mech.* **858**, 917–948.

DICKINSON, M. H., LEHMANN, F. O. & SANE, P. O. 1999 Wing rotation and the aerodynamic basis of insect flight. *Science* **284** (5422), 1954–1960.

https://doi.org/10.1017/jfm.2019.735 Published online by Cambridge University Press

ELDREDGE, J. D. & DARAKANANDA, D. 2015 Reduced-order two- and three-dimensional vortex modeling of unsteady separated flows. In *53rd AIAA Aerospace Sciences Meeting*. AIAA SciTech Forum (2015-1749).

ELDREDGE, J. D. & JONES, A. R. 2019 Leading-edge vortices: mechanics and modeling. *Annu. Rev. Fluid Mech.* **51**, 75–104.

GALLER, J. N., WEYMOUTH, G. D. & RIVAL, D. E. 2019 Progress towards modelling unsteady forces using a drift-volume approach. In *57th AIAA Aerospace Sciences Meeting*. AIAA SciTech Forum (2019-1147).

GARMANN, D. J. & VISBAL, M. R. 2014 Dynamics of revolving wings for various aspect ratios. *J. Fluid Mech.* **748**, 932–956.

GHARIB, M., RAMBOD, E. & SHARIFF, K. 1998 A universal time scale for vortex ring formation. *J. Fluid Mech.* **360**, 121–140.

HARBIG, R. R., SHERIDAN, J. & THOMPSON, M. C. 2013 Reynolds number and aspect ratio effects on the leading-edge vortex for rotating insect wing planforms. *J. Fluid Mech.* **717**, 166–192.

HEMATI, M. S., ELDREDGE, J. D. & SPEYER, J. L. 2014 Improving vortex models via optimal control theory. *J. Fluids Struct.* **49**, 99–111.

JARDIN, T. & COLONIUS, T. 2018 On the lift-optimal aspect ratio of a revolving wing at low Reynolds number. *J. R. Soc. Interface* **15** (143), 20170933.

JARDIN, T., FARCY, A. & DAVID, L. 2012 Three-dimensional effects in hovering flapping flight. *J. Fluid Mech.* **702**, 102–125.

JIAO, Z., ZHAO, L., SHANG, Y. & SUN, X. 2018 Generic analytical thrust-force model for flapping wings. *AIAA J.* **56** (2), 581–593.

JONES, A. R. & BABINSKY, H. 2011 Reynolds number effects on leading edge vortex development on a waving wing. *Exp. Fluids* **51** (1), 197–210.

JONES, A. R., MANAR, F., PHILLIPS, N., NAKATA, T., BOMPHREY, R., RINGUETTE, M. J., PERCIN, M., VAN OUDHEUSDEN, B. & PALMER, J. 2016 Leading edge vortex evolution and lift production on rotating wings (invited). In *54th AIAA Aerospace Sciences Meeting*. AIAA SciTech Forum (2016-0288).

VON KÁRMÁN, T. & SEARS, W. R. 1938 Airfoil theory for non-uniform motion. *J. Aeronaut. Sci.* **5** (10), 379–390.

KIM, D. & GHARIB, M. 2010 Experimental study of three-dimensional vortex structures in translating and rotating plates. *Exp. Fluids* **49** (1), 329–339.

KRUYT, J. W., VAN HEIJST, G. F., ALTSHULER, D. L. & LENTINK, D. 2015 Power reduction and the radial limit of stall delay in revolving wings of different aspect ratio. *J. R. Soc. Interface* **12**, 20150051.

LEE, J., CHOI, H. & KIM, H. Y. 2015 A scaling law for the lift of hovering insects. *J. Fluid Mech.* **782**, 479–490.

LEE, Y. J., LUA, K. B. & LIM, T. T. 2016*a* Aspect ratio effects on revolving wings with Rossby number consideration. *Bioinspir. Biomim.* **11**, 056013.

LEE, Y. J., LUA, K. B., LIM, T. T. & YEO, K. S. 2016*b* A quasi-steady aerodynamic model for flapping flight with improved adaptability. *Bioinspir. Biomim.* **11**, 036005.

LENTINK, D. & DICKINSON, M. H. 2009 Rotational accelerations stabilize leading edge vortices on revolving fly wings. *J. Expl Biol.* **212**, 2705–2719.

LI, C., DONG, H. & CHENG, B. 2017 Effects of aspect ratio and angle of attack on tip vortex structures and aerodynamic performance for rotating flat plates. In *47th AIAA Fluid Dynamics Conference*. AIAA Aviation Forum (2017-3645).

LI, J. & WU, Z.-N. 2016 A vortex force study for a flat plate at high angle of attack. *J. Fluid Mech.* **801**, 222–249.

LIMACHER, E., MORTON, C. & WOOD, D. 2016 On the trajectory of leading-edge vortices under the influence of coriolis acceleration. *J. Fluid Mech.* **800**, R1.

MANAR, F. H., MANCINI, P., MAYO, D. & JONES, A. R. 2016 Comparison of rotating and translating wings: force production and vortex characteristics. *AIAA J.* **54** (2), 519–530.

MANCINI, P., MANAR, F. H. & JONES, A. R. 2015 A semi-empirical approach to modeling lift production. In *53rd AIAA Aerospace Sciences Meeting*. AIAA SciTech Forum (2015-1748).

https://doi.org/10.1017/jfm.2019.735 Published online by Cambridge University Press

NABAWY, M. R. A. & CROWTHER, W. J. 2014 On the quasi-steady aerodynamics of normal hovering flight part II: model implementation and evaluation. *J. R. Soc. Interface* **11**, 20131197.

NGUYEN, A. T., KIM, J.-K., HAN, J.-S. & HAN, J.-H. 2016 Extended unsteady vortex-lattice method for insect flapping wings. *J. Aircraft* **53** (6), 1709–1718.

OL, M. & BABINSKY, H. 2016 Extensions of fundamental flow physics to practical MAV aerodynamics. *Tech. Rep.* TR-AVT-202. NATO STO.

OZEN, C. A. & ROCKWELL, D. 2012*a* Flow structure on a rotating plate. *Exp. Fluids* **52**, 207–223.

OZEN, C. A. & ROCKWELL, D. 2012*b* Three-dimensional vortex structure on a rotating wing. *J. Fluid Mech.* **707**, 541–550.

PEDERSEN, C. B. & ŻBIKOWSKI, R. 2006 An indicial-Polhamus aerodynamic model of insect-like flapping wings in hover. In *Flow Phenomena in Nature* (ed. R. Liebe), Design and Nature, vol. 2, pp. 606–665. WIT Press.

PERCIN, M. & VAN OUDHEUSDEN, B. W. 2015 Three-dimensional flow structures and unsteady forces on pitching and surging revolving flat plates. *Exp. Fluids* **56**, 47.

PHILLIPS, N., KNOWLES, K. & BOMPHREY, R. J. 2015 The effect of aspect ratio on the leading-edge vortex over an insect-like flapping wing. *Bioinspir. Biomim.* **10** (5), 056020.

PITT FORD, C. W. & BABINSKY, H. 2013 Lift and the leading-edge vortex. *J. Fluid Mech.* **720**, 280–313.

POLHAMUS, E. C. 1966 A concept of the vortex lift of sharp-edge delta wings based on a leading-edge-suction analogy. *NASA Tech. Rep.* TN D-3767.

PULLIN, D. I. & WANG, Z. J. 2004 Unsteady forces on an accelerating plate and application to hovering insect flight. *J. Fluid Mech.* **509**, 1–21.

RAMESH, K., GOPALARATHNAM, A., GRANLUND, K., OL, M. V. & EDWARDS, J. R. 2014 Discrete-vortex method with novel shedding criterion for unsteady aerofoil flows with intermittent leading-edge vortex shedding. *J. Fluid Mech.* **751**, 500–538.

ROCCIA, B. A., PREIDIKMAN, S., MASSA, J. C. & MOOK, D. T. 2013 Modified unsteady vortex-lattice method to study flapping wings in hover flight. *AIAA J.* **51** (11), 2628–2642.

SANE, S. P. & DICKINSON, M. H. 2002 The aerodynamic effects of wing rotation and a revised quasi-steady model of flapping flight. *J. Expl Biol.* **205**, 1087–1096.

SEDOV, L. 1965 *Two-Dimensional Problems in Hydrodynamics and Aerodynamics*. Interscience.

SHARIFF, K. & LEONARD, A. 1992 Vortex rings. *Annu. Rev. Fluid Mech.* **24** (1), 235–279.

SULLIVAN, I. S., NIEMELA, J. J., HERSHBERGER, R. E., BOLSTER, D. & DONNELLY, R. J. 2008 Dynamics of thin vortex rings. *J. Fluid Mech.* **609**, 319–347.

SUN, M. & WU, J. 2004 Large aerodynamic forces on a sweeping wing at low Reynolds number. *Acta Mechanica Sin.* **20**, 24.

TAHA, H. E., HAJJA, M. R. & BERAN, P. S. 2014 State-space representation of the unsteady aerodynamics of flapping flight. *Aerosp. Sci. Technol.* **34**, 1–11.

THEODORSEN, T. 1935 General theory of aerodynamic instability and the mechanism of flutter. *NACA Tech. Rep.* 496.

WAGNER, H. 1925 Über die entstehung des dynamischen auftriebs von tragflügeln. *Z. Angew. Math. Mech.* **5**, 17–35.

WANG, C. & ELDREDGE, J. D. 2013 Low-order phenomenological modeling of leading-edge vortex formation. *Theor. Comput. Fluid Dyn.* **27**, 577–598.

WOLFINGER, M. & ROCKWELL, D. 2015 Transformation of flow structure on a rotating wing due to variation of radius of gyration. *Exp. Fluids* **56** (137), 1–18.

WONG, J. G., GILLESPIE, G. & RIVAL, D. E. 2018 Circulation redistribution in leading-edge vortices with spanwise flow. *AIAA J.* **56** (10), 3857–3862.

WU, J.-Z., MA, H. Y. & ZHOU, M. D. 2006 *Vorticity and Vortex Dynamics*. Springer.

XIA, X. & MOHSENI, K. 2013 Lift evaluation of a two-dimensional pitching flat plate. *Phys. Fluids* **25**, 091901.

YAN, Z., TAHA, H. E. & HAJJA, M. R. 2014 Geometrically-exact unsteady model for airfoils undergoing large amplitude maneuvers. *Aerosp. Sci. Technol.* **39**, 293–306.

ŻBIKOWSKI, R. 2002 On aerodynamic modelling of an insect-like flapping wing in hover for micro air vehicles. *Phil. Trans. R. Soc. Lond.* A **360** (1791), 273–290.

https://doi.org/10.1017/jfm.2019.735 Published online by Cambridge University Press